Supplementary Materials for

Implications of Giant Ooids for the Carbonate Chemistry of Early Triassic Seawater

Xiaowei Li[1], Elizabeth J. Trower[2], Daniel J. Lehrmann[3], Marcello Minzoni[4], Brian M. Kelley[5], Ellen K. Schaal[6], Demir Altiner[7], Meiyi Yu[8], Jonathan L. Payne[1]

[1]*Department of Geological Sciences, Stanford University, Stanford, CA 94305, USA;*

[2]*Department of Geological Sciences, University of Colorado Boulder, Boulder, CO 80309, USA*

[3]*Department of Geosciences, Trinity University, San Antonio, TX 78212, USA*

[4]*Department of Geological Sciences, University of Alabama, Tuscaloosa, AL 35487, USA*

[5]*Department of Geosciences, Pennsylvania State University, PA 16802, USA*

[6]*Department of Environmental Science & Studies, DePaul University, Chicago, IL 60604, USA*

[7]*Department of Geological Engineering, Middle East Technical University, Ankara 06800, Turkey*

[8]*Department of Resources & Environmental Engineering, Guizhou University, Guiyang, Guizhou 550025, PRC*

This study applies a physicochemical model for ooid formation described in Trower et al. (2017) to determine the range of seawater conditions compatible with the formation of giant ooids (>2 mm in diameter) during Early Triassic time. Because the model is already published, we focus here on the selection of boundary conditions (i.e., parameter values) used in this study, which includes a broader exploration of parameter space than conducted by Trower et al. (2017).

The supplementary materials include six supporting subsections (Text S1 to S6), six supporting figures (Figures S1 to S6), and one supporting table (Table S1).

TEXT S1. GEOLOGIC SETTING AND AGES OF SAMPLES

The Great Bank of Guizhou (GBG) initiated in the latest Permian, Changhsingian, on antecedent topography inherited from the south-facing shelf margin of the Yangtze Platform (YP) composed of sponge-microbialite boundstone (Fig. S1A; Lehrmann et al., 1998; Li et al., 2012). By the end of Induan time (252.2 - 251.2 Ma), the GBG was a high-relief platform with oolite shoals developed at the margin and had slopes with approximately 300 m of relief above the adjacent basin floor. Facies in the platform interior grade upward from microbial boundstone to thin-bedded lime mudstone and, subsequently, to peritidal cyclic limestone. Marginal shoal facies comprise oolitic grainstone with subordinate molluscan packstone (Lehrmann et al., 1998; Fig. S1A). Coeval slope facies are composed of shale, punctuated by an upward-increasing occurrence of carbonate debris-flow breccia, carbonate turbidites, and periplatform pelagic lime mudstone. Carbonate breccias and carbonate turbidites were primarily sourced from aggradational oolitic shoals at the platform margin (Lehrmann et al., 1998; Fig. S1A). Continued aggradation of the margin during the Olenekian (251.2 - 247.2 Ma) generated a high-relief (~900 m) carbonate platform with steep, accretionary slope clinoforms (Kelley, 2014; Fig. S1A). Ooid shoals remained common on the platform margin during Olenekian time. The coeval platform interior consists of dolomitized peritidal limestone (Lehrmann et al., 1998; Kelley, 2014). Carbonate debris-flow breccia and carbonate turbidites on the slope contains clasts of margin-derived oolite indicating continued shedding to the slope of oolite material from the margin.

The YP at the Zhenfeng margin consisted of a ramp during the Induan (Fig. S1B; Minzoni et al., 2013). The inner ramp is composed of interbedded lime mudstone and siltstone with ooid shoals (Fig. S1B). The facies grade basinward into outer ramp mud-dominated facies containing slumps, carbonate turbidites, and debris-flow breccia. The Induan ramp grades upward into a low-relief bank in the Olenekian accompanied by marked progradation and slight aggradation of the ooid shoal complex (Fig. S1B). The Olenekian platform interior consists of subtidal to peritidal cyclic dolomite. Coeval adjacent slope and basin strata primarily consist of lime mudstone and carbonate debris-flow breccia and carbonate turbidites (Fig. S1B; Minzoni et al., 2013).

The Chongzuo-Pingguo Platform (CPP) is the largest isolated platform in the Nanpanjiang Basin (Fig. 1C). The Pingxiang-Dongmen fault offsets the southern margin in the Late Permian and was reactivated during the Cretaceous (Fig. S1C; Lehrmann et al., 2007). In the Early Triassic, the CPP evolved as a low-relief bank with a gentle slope at its flanks. The platform interior is composed primarily of oolitic packstone-grainstone and lime mudstone. A thicker succession of oolite containing giant ooids reflects shoals that formed at the bank margins. The basin-margin slopes are dominated by lime mudstone, carbonate debris-flow breccia and carbonate turbidites. (Fig. S1C).

The ages of samples in this study (middle Griesbachian and middle Dienerian; Fig. 2D) are constrained by carbon isotope chemostratigraphy ($\delta^{13}C_{\_VPDB}$ = 3.32‰ for sample DXR-3 collected from the GBG, $\delta^{13}C_{\_VPDB}$ = 1.5‰ for sample M1 from Zhenfeng of the YP; and $\delta^{13}C_{\_VPDB}$ = - 0.56‰ for sample PG-34 that was collected in the upper portion of the Majiaoling Formation (Dienerian) in the CPP reported by Lehrmann et al. 2012) and foraminiferan biostratigraphy (*Postcladella grandis* present in sample M1 from Zhenfeng and *Postcladella* present in sample DXR-3 from the GBG; Fig. S2).

TEXT S2. ARAGONITE OR CALCITE PRECIPITATION RATE

The aragonite or calcite precipitation rate (P) can be expressed as a function of the carbonate saturation state of seawater, Ω (Zhong and Mucci, 1989),

$$P = k\ (\Omega - 1)^n, \quad (1)$$

in which the rate constant, k in μmol/m^2/hr, and the reaction order, n, can change with solution chemistry, reaction mechanism, and surface properties (Burton and Walter, 1987; Zhong and Mucci, 1989; Morse et al., 2007). The values of k and n values are influenced by temperature and salinity; within the range of reasonable values for Triassic seawater, they are more sensitive to temperature than to salinity (Burton and Walter, 1987; Zhong and Mucci, 1989). Therefore, we used values of k = 45.1 μmol/m^2/hr and n = 2.4 for aragonite and k = 3.7 μmol/m^2/hr and n = 2.3 for calcite at 37 °C from Burton and Walter (1987) to predict aragonite and calcite precipitation (Fig. 3). We used these values because the temperature is close to the Early Triassic seawater temperature indicated by oxygen isotope proxy data (Sun et al., 2012). Sensitivity analysis was conducted using values appropriate to 25 °C (k = 40.6 μmol/m^2/hr and n = 1.7 for aragonite and k = 3.9 μmol/m^2/hr and n = 1.9 for calcite) to test how temperature would influence the simulation results (Fig. S4; Burton and Walter, 1987). At lower temperatures, more extreme Ω is needed at in order to form ooids of the same sizes due to the slower kinetics of precipitation (see Figure 3 for comparison).

TEXT S3. PARTICLE SURFACE AREA

Trower et al. (2017) adopted a specific surface area estimate based on measurements of coral particles (Walter and Morse, 1984) because of similarities in surface microstructure between ooids and coral particles:

$$A_{surface} = 1/6\ \pi D^3 * \rho_{ooid} * SSA, \quad (2)$$

where specific surface area, *SSA*, given in m^2/g, is a function of ooid diameter (D) and density (ρ_{ooid}). For ρ_{ooid}, we used a value equal to the density of aragonite or calcite because petrographic observations indicate that Lower Triassic ooids were bimineralic (Lehrmann et al., 2012; Fig. 2G & H). We used a value of SSA = 30.8 because its corresponding coral particle size is close to the size range of giant ooids in this study (Walter and Morse, 1984).

TEXT S4. BED SHEAR VELOCITY

In the modern ocean, ooids commonly occur in high-energy environments where grains are transported near or beyond the threshold of suspension (e.g. Trower et al., 2018). Early Triassic ooid sizes and transport modes can be used to determine likely ranges of bed shear velocity (u_*) that would be necessary for giant ooids to be transported in bed load or suspended load. Sediment transport mode can be estimated using the Rouse number, $P = w_s / (\kappa\, u_*)$, where w_s is settling velocity, calculated following Dietrich (1982), and $\kappa = 0.41$ is the dimensionless von Karman constant. $P > 2.5$ corresponds to bed load transport; $2.5 > P > 1.2$ corresponds to ~50% suspended load transport; $1.2 > P > 0.8$ corresponds to ~100% suspended load transport; and $P < 0.8$ corresponds to washload transport. For the largest ooid diameter measured in this study (D = 9.3 mm), $w_s \approx 0.75$ m/s for ooids composed of aragonite (≈ 0.72 m/s for calcite), and $P = 1.2$ corresponds with $u_* = 1.5$ m/s, a conservative upper bound on bed shear velocities in giant ooid-forming environments (Figs. S5 and S6).

Equilibrium ooid size also depends on u_* due to the offsetting effects of impact frequency (higher for bed load transport) and impact energy (higher for suspended load transport). Because abrasion rate is minimized for u_* corresponding to the threshold of motion (P just less than 2.5) due to these effects, equilibrium ooid size is maximized at u_* closer to or at the threshold of suspension for giant ooids (Figs. S5 and S6). This transport mode-dependent effect on equilibrium ooid size is generally smaller than the effects of changing Ω or f within the range of plausible values (Figs. S5 and S6).

TEXT S5. KINEMATIC VISCOSITY OF EARLY TRIASSIC TROPICAL SURFACE WATER

In the model of Trower et al. (2017), density and kinematic viscosity of seawater must be specified because they affect sediment transport mode and, therefore, abrasion rate. Density (ρ, in kg/m^3), dynamic viscosity (μ, in kg/(ms)), and kinematic viscosity (γ, in m^2/s) of Early Triassic seawater are functions of temperature (T, °C) and salinity (Sal, ppm) (El-Dessouky and Ettouney, 2002) as expressed by

$$\rho = 10^3 (A_1F_1 + A_2F_2 + A_3F_3 + A_4F_4), \quad (3)$$

where

$$A_1 = 4.032219G_1 + 0.115313G_2 + 3.26 * 10^{-4} G_3, \quad (4)$$

$$A_2 = -0.108199G_1 + 1.571*10^{-3}G_2 - 4.23*10^{-4} G_3, \quad (5)$$

$$A_3 = -0.012247G_1 + 1.74*10^{-3}G_2 - 9*10^{-6} G_3, \quad (6)$$

$$A_4 = 6.92*10^{-4}G_1 - 8.7*10^{-5}G_2 - 5.3*10^{-5}G_3, \quad (7)$$

$$F_1 = 0.5,\ F_2 = A,\ F_3 = 2A^2 - 1,\ F_4 = 4A^3 - 3A, \quad (8)$$

$$G_1 = 0.5,\ G_2 = B,\ G_3 = 2B^2 - 1, \quad (9)$$

$$A = (2T - 200)/160, \quad (10)$$

$$B = (2Sal/1000 - 150)/150. \quad (11)$$

A_1 to A_4, F_1 to F_4, G_1 to G_3, A, and B in Equations (3) to (11) above are parameters defining an empirical fit of seawater density as a function of salinity and temperature. Early Triassic surface ocean temperatures in the area of the south China block were in the range of 33 to 38 °C based on the oxygen isotope composition of biogenic apatite from conodont microfossils (Sun et al., 2012). We use 36 °C to represent the average temperature in the Early Triassic in this study because it is generally consistent with the sea surface temperatures in the middle-upper Griesbachian, middle-upper Dienerian, upper Smithian, and upper Spathian (Li et al., 2015; Tian et al., 2015; Fang et al., 2017). Coeval salinity was approximately 41‰ based on data from fluid inclusions in halite (Hay et al., 2006). Therefore, according to Equations (3) to (11), ρ was approximately 1023.7 kg/m^3. The modeling results are not substantially affected by the use of any reasonable value for temperature and salinity within the range reported in Sun et al. (2012) and Hay et al. (2006).

The relationship between μ and γ is:

$\gamma = \mu / \rho$, (12)

$\mu = (\mu_W)(\mu_R)*10^{-3}$, (13)

where:

$Ln\ (\mu_W) = -3.79418 + 604.129 / (139.18 + T)$, (14)

$\mu_R = 1 + C*Sal + D*Sal^2$, (15)

$C = 1.474*10^{-3} + 1.5*10^{-5}T - 3.927*10^{-8}T^2$, (16)

$D = 1.0734*10^{-5} - 8.5*10^{-8}T + 2.23*10^{-10}T^2$. (17)

Thus, γ is 0.756 * 10^{-6} m^2/s, according to Equations (12) through (17).

TEXT S6. CRITICAL SHIELDS STRESS FOR INITIAL SEDIMENT MOTION

A critical Shields number (0.03) for initial motion of ooids smaller than gravel-size was used in Trower et al. (2017). Because the size of Early Triassic giant ooids in this study ranges from 2 to approximately 9 mm (Fig. 2A to C), we used three different critical Shields numbers for corresponding sizes of giant ooids (Table S1; Berenbrock and Tranmer, 2008).

TABLE S1. CRITICAL SHIELDS NUMBER VARIES WITH RANGES OF PARTICLE DIAMETERS

Particle classification name	Ranges of particle diameters (mm)	Critical Shields number
Medium gravel	8 - 16	0.045
Fine gravel	4 - 8	0.043
Very fine gravel	2 - 4	0.040
sand	<2	0.030

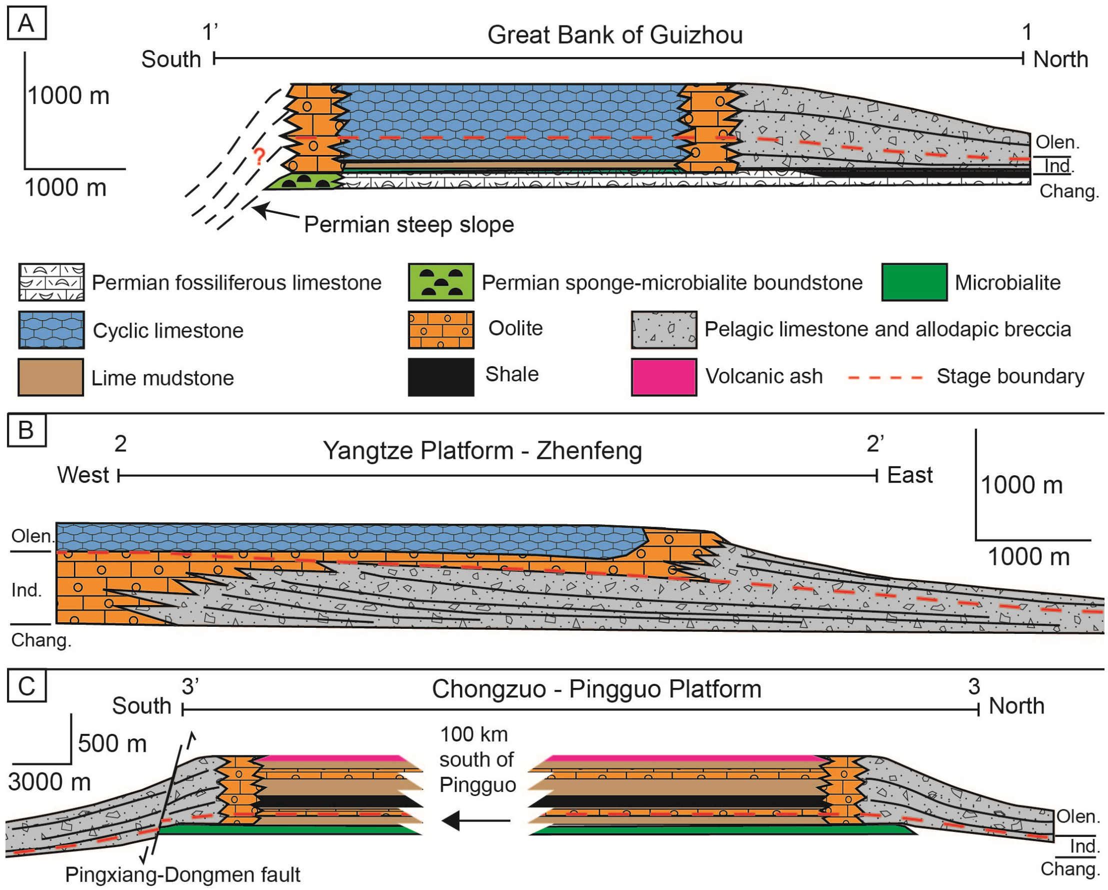

Figure S1. Schematic Early Triassic architecture of (A) the GBG, (B) the YP at Zhenfeng, and (C) the CPP. Modified after Lehrmann et al. (1998, 2012) and Minzoni et al. (2013). The geological map of the GBG contains new data from field mapping conducted by X. Li and D. Lehrmann, including oolite grainstone deposited above the antecedent topography of the southern margin, Upper Permian sponge-microbialite boundstone. Abbreviations of stages: Chang. = Changhsingian (Upper Permian), Ind. = Induan (Lower Triassic), Olen. = Olenekian (Lower Triassic). Ooids are developed at the platform margin of the GBG, YP, and CPP in the Early Triassic, but giant ooids have been only reported from middle-upper Griesbachian, middle-upper Dienerian, upper Smithian, and upper Spathian (Li et al., 2015; Tian et al., 2015; Fang et al., 2017; also see Fig. 2D).

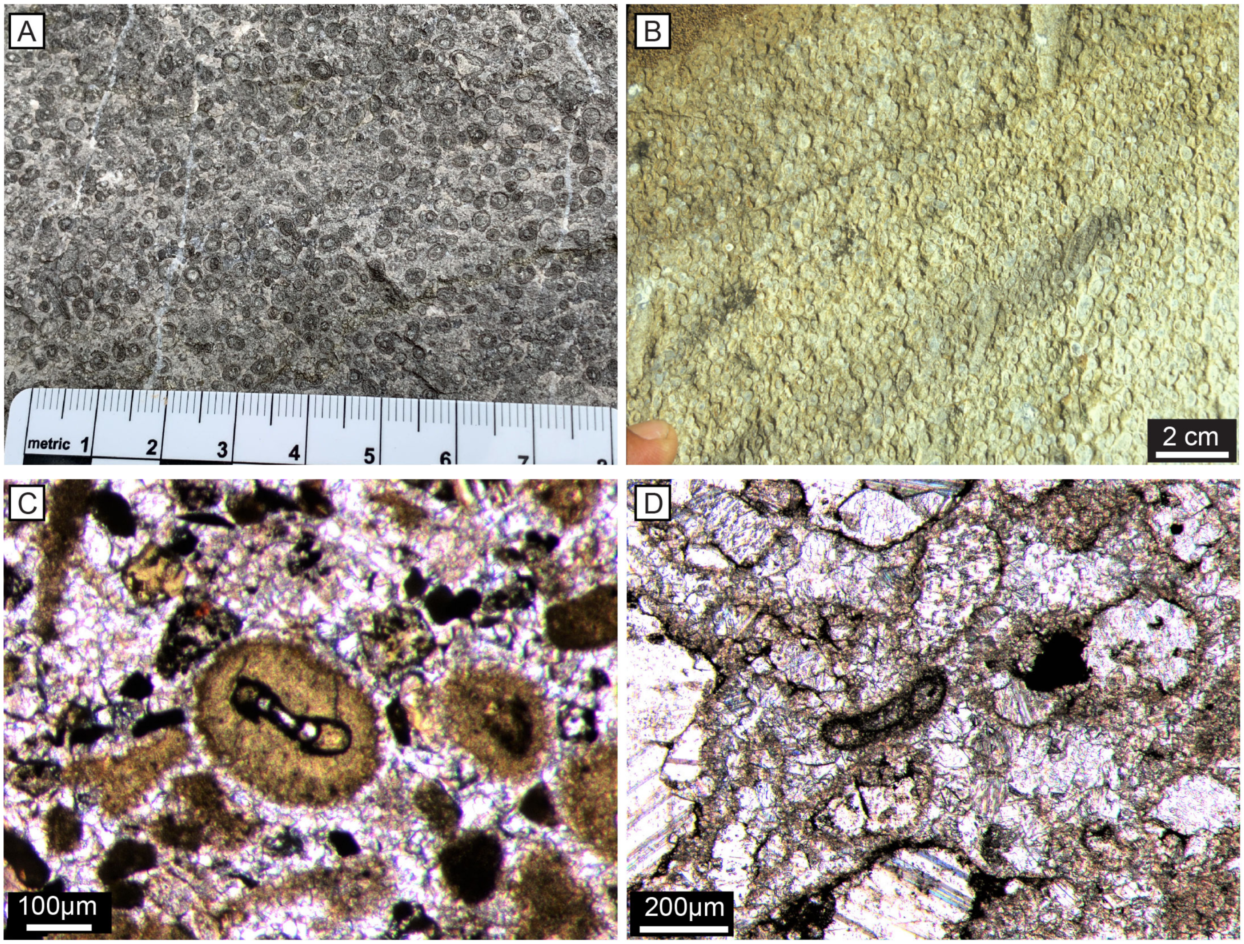

Figure S2. Outcrop of the Lower Triassic giant ooids and photomicrographs of foraminifers. A: An outcrop image of giant ooids at the Zhenfeng margin of the Yangtze Platform. B: An outcrop image displaying giant ooids from the northern margin of Chongzuo-Pingguo Platform. C: Foraminifer *Postcladella grandis* of Griesbachian age, present in sample M1 from Zhenfeng of Yangtze Platform. D: Foraminifer *Postcladella* of Griesbachian to Dienerian age, found in sample DXR-3 from the Great Bank of Guizhou.

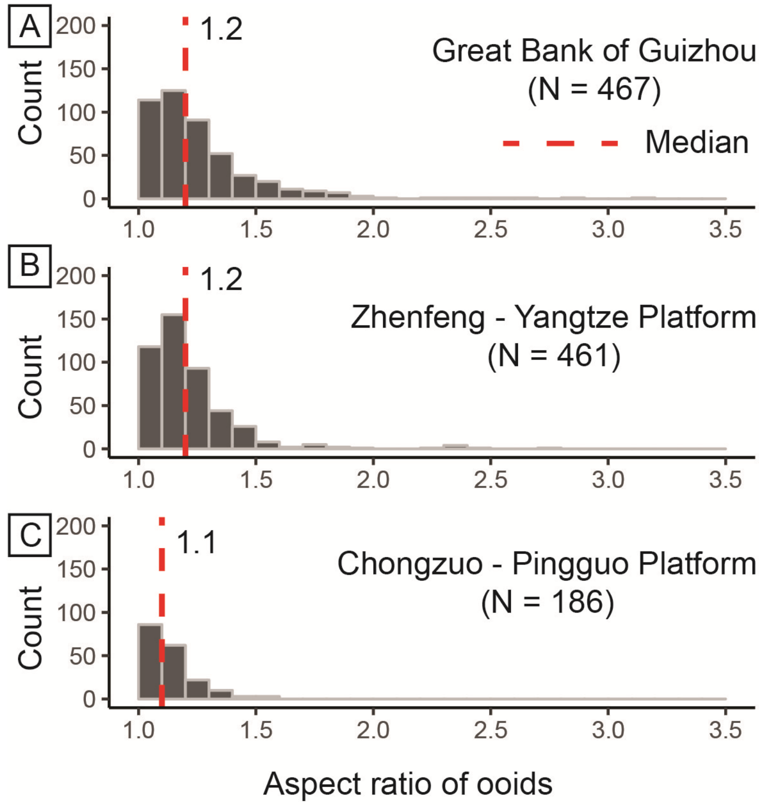

Figure S3. Aspect ratios of Early Triassic giant ooids from the GBG (A), YP (B), and CPP (C), showing values consistent with saltation or suspension transport rather than rolling or sliding as the transport modes of giant ooids (Sipos et al., 2018).

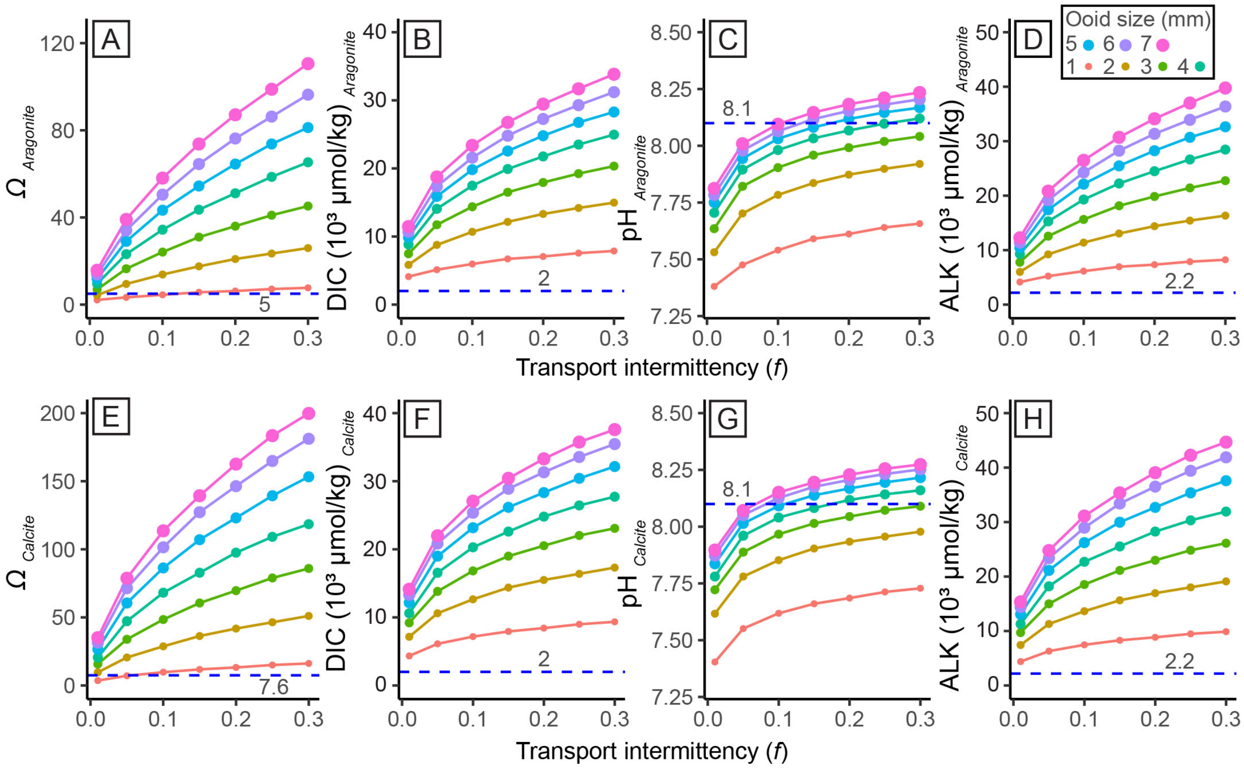

Figure S4. Modeling results of chemical properties of seawater chemistry required for giant ooid formation at 25°C. Horizontal dashed lines represent modern tropical long-term average values of surface seawater from the Little Bahamas Bank, Turks and Caicos Islands, and tropical open ocean (Bustos-Serrano et al., 2009; Jiang et al., 2015; Trower et al., 2018). Values of kinetic parameters of aragonite and calcite precipitation at 25°C are lower than at 37°C (Table 1 in Burton and Walter, 1987; also see Fig. 3A to H for comparison). A-D represent results assuming an aragonite polymorph (k = 40.6 μmol/m^2/hr, n = 1.7, pCO$_2$ = 4000 ppm); E-H represent results assuming a calcite polymorph (k = 3.9 μmol/m^2/hr, n = 1.9, pCO$_2$ = 4000 ppm). A: Aragonite saturation state ($\Omega_{Aragonite}$). B: Dissolved inorganic carbon (DIC $_{Aragonite}$). C: Acidity (pH $_{Aragonite}$). D: Total alkalinity (ALK $_{Aragonite}$). E: Calcite saturation state ($\Omega_{Calcite}$). The value of modern calcite saturation state (7.6) is converted from aragonite saturation state (~5) in modern tropical ocean based on (Mucci, 1983). F: Dissolved inorganic carbon (DIC $_{Calcite}$). G: Acidity (pH $_{Calcite}$). H: Total alkalinity (ALK $_{Calcite}$).

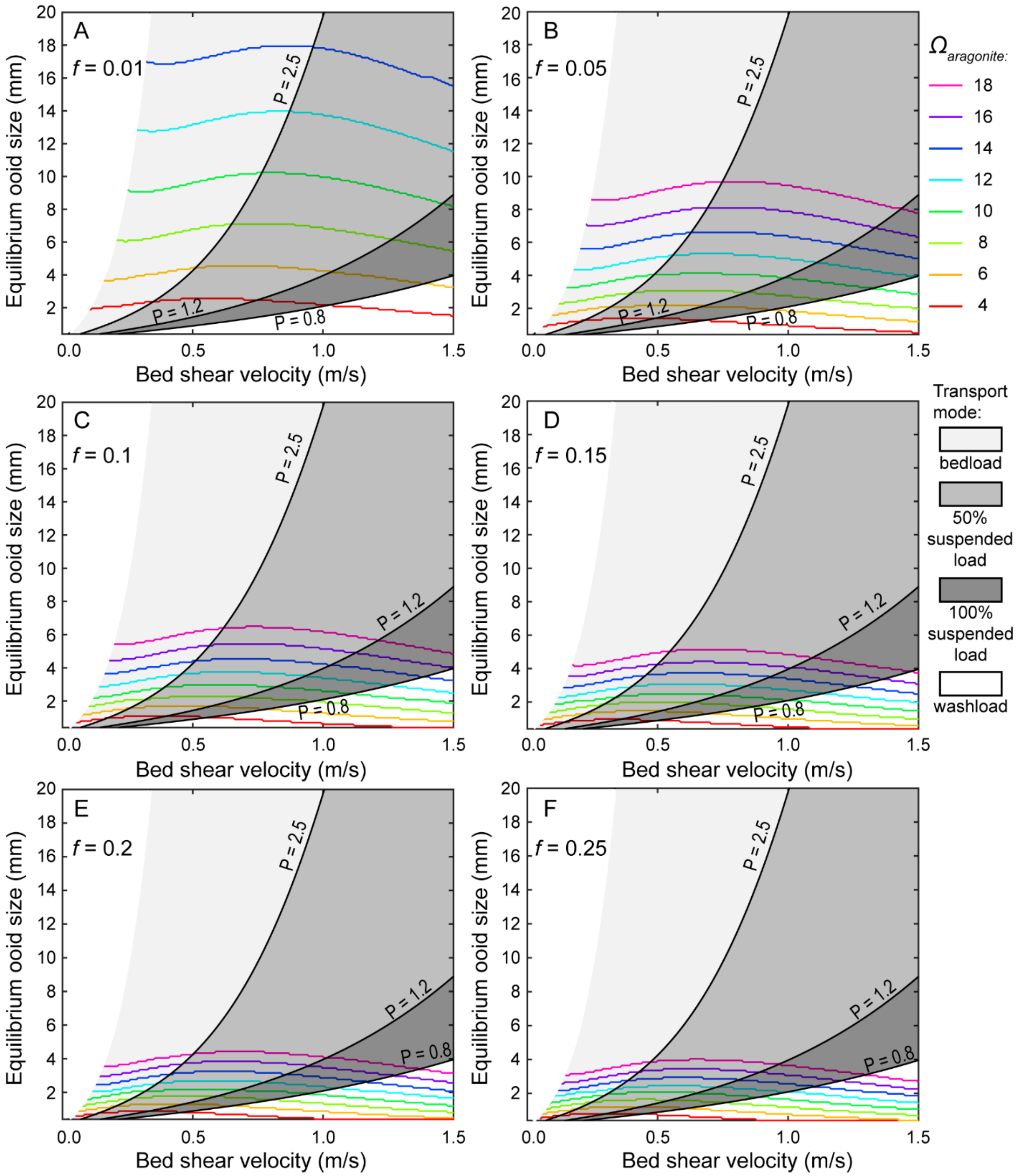

Figure S5. Predicted equilibrium ooid size versus bed shear velocity (u_*) for a range of aragonite saturation state ($\Omega_{Aragonite}$) and transport intermittency (f) when temperature is at 36 °C. Transport modes are indicated by Rouse number curve (P, black curves). The model predicts that equilibrium ooid size can be increased by increasing $\Omega_{Aragonite}$, decreasing f, or getting u_* approach closer to or at the threshold of suspension.

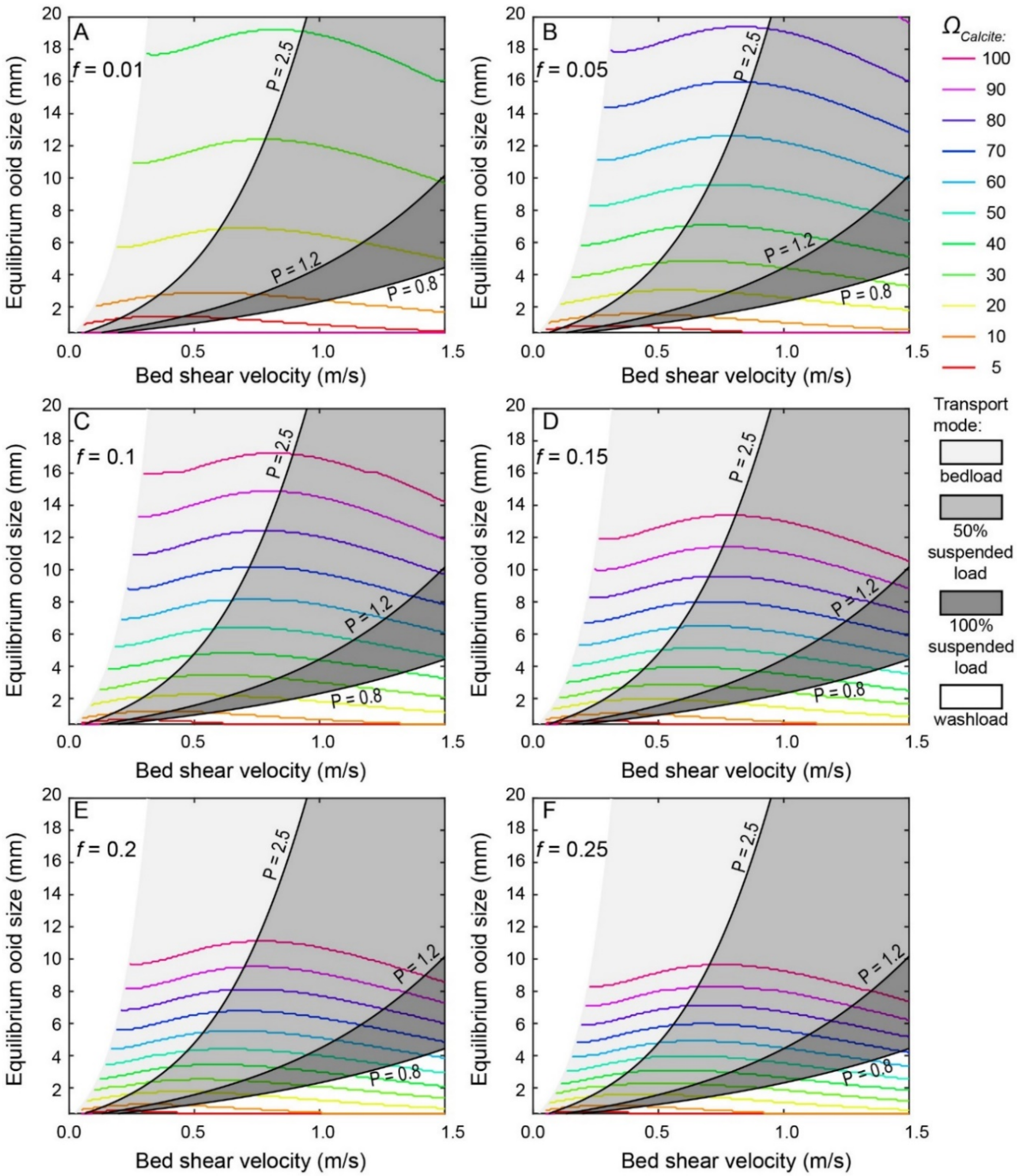

Figure S6. Predicted equilibrium ooid size vs. bed shear velocity (u_*) for a range of calcite saturation state ($\Omega_{Calcite}$) and transport intermittency (f) when temperature is at 36 °C. Transport modes are indicated by Rouse number curve (P, black curves). The model predicts that equilibrium ooid size can be increased by increasing $\Omega_{Calcite}$, decreasing f, or getting u_* approach closer to or at the threshold of suspension.

REFERENCES CITED

Berenbrock, C., and Tranmer, A.W., 2008, Simulation of flow, sediment transport, and sediment mobility of the Lower Coeur d'Alene River, Idaho: U.S. Geological Survey Scientific Investigations Report 2008-5093, 43 p.

Burton, E.A., and Walter, L.M., 1987, Relative precipitation rates of aragonite and Mg calcite from seawater: Temperature or carbonate ion control? Geology, v. 15, p. 111–114, doi:10.1130/0091-7613(1987)15<111:RPROAA>2.0.CO;2.

Bustos-Serrano, H., Morse, J.W., and Millero, F.J., 2009, The formation of whitings on the Little Bahama Bank: Marine Chemistry, v. 113, p. 1–8, doi:10.1016/j.marchem.2008.10.006.

Dietrich, W.E., 1982, Settling velocity of natural particles: Water Resources Research, v. 18, p. 1615–1626, doi:10.1029/WR018i006p01615.

El-Dessouky, H.T., and Ettouney, H.M., 2002, Fundamentals of salt water desalination: Elsevier Science B.V., 525–564 p.

Fang, Y., Chen, Z.Q., Kershaw, S., Li, Y., and Luo, M., 2017, An Early Triassic (Smithian) stromatolite associated with giant ooid banks from Lichuan (Hubei Province), South China:

Environment and controls on its formation: Palaeogeography, Palaeoclimatology, Palaeoecology, v. 486, p. 108–122, doi:10.1016/j.palaeo.2017.02.006.

Hay, W.W., Migdisov, A., Balukhovsky, A.N., Wold, C.N., Flögel, S., and Söding, E., 2006, Evaporites and the salinity of the ocean during the Phanerozoic: Implications for climate, ocean circulation and life: Palaeogeography, Palaeoclimatology, Palaeoecology, v. 240, p. 3–46, doi:10.1016/j.palaeo.2006.03.044.

Jiang, L., Feely, R.A., Carter, B.R., Greeley, D.J., Gledhill, D.K., and Arzayus, K.M., 2015, Climatological distribution of aragonite saturation state in the global oceans: Global Biogeochemical Cycles, p. 1656–1673, doi:10.1002/2015GB005198.

Kelley, B.M., 2014, Physical, chemical, and biological controls on the stratigraphic evolution and spatial variability of an isolated carbonate platform [Ph.D. thesis]: Stanford University, 1–51 p.

Lehrmann, D.J. et al., 2007, Impact of differential tectonic subsidence on isolated carbonate-platform evolution: Triassic of the Nanpanjiang Basin, south china: AAPG Bulletin, v. 91, p. 287–320, doi:10.1306/10160606065.

Lehrmann, D.J., Minzoni, M., Li, X., Yu, M., Payne, J.L., Kelley, B.M., Schaal, E.K., and Enos, P., 2012, Lower Triassic oolites of the Nanpanjiang Basin, south China: Facies architecture, giant ooids, and diagenesis-implications for hydrocarbon reservoirs: AAPG Bulletin, v. 96, doi:10.1306/01231211148.

Lehrmann, D.J., Wei Jiayong, and Enos, P., 1998, Controls on facies architecture of a large Triassic carbonate platform; the Great Bank of Guizhou, Nanpanjiang Basin, south China: Journal of Sedimentary Research, v. 68, p. 311–326, doi:10.2110/jsr.68.311.

Li, F., Yan, J., Chen, Z.Q., Ogg, J.G., Tian, L., Korngreen, D., Liu, K., Ma, Z., and Woods, A.D., 2015, Global oolite deposits across the Permian-Triassic boundary: A synthesis and implications for palaeoceanography immediately after the end-Permian biocrisis: Earth-Science Reviews, v. 149, p. 163–180, doi:10.1016/j.earscirev.2014.12.006.

Li, X., Yu, M., Lehrmann, D.J., Payne, J.L., Kelley, B.M., and Minzoni, M., 2012, Factors controlling carbonate platform asymmetry: Preliminary results from the Great Bank of Guizhou, an isolated Permian-Triassic Platform in the Nanpanjiang Basin, south China: Palaeogeography, Palaeoclimatology, Palaeoecology, v. 315–316, p. 158–171, doi:10.1016/j.palaeo.2011.11.023.

Minzoni, M. et al., 2013, Triassic tank: Platform margin and slope architecture in space and time, Nanpanjiang Basin, south China, *in* Verwer, K., Playton, T.E., and Harris, P.M. (Mitch) eds., Deposits, Architecture, and Controls of Carbonate Margin, Slope and Basinal Settings, SEPM Special Publication 105, p. 84–113, doi:10.2110/sepmsp.105.10.

Morse, J.W., Arvidson, R.S., and Lüttge, A., 2007, Calcium carbonate formation and dissolution: Chemical Reviews, v. 107, p. 342–381, doi:10.1021/cr050358j.

Mucci, A., 1983, The solubility of calcite and aragonite in seawater at various salinities, temperatures, and one atmosphere total pressure: American Journal of Science, v. 283, p. 780–799, doi:10.2475/ajs.283.7.780.

Sipos, A.A., Domokos, G., and Jerolmack, D.J., 2018, Shape evolution of ooids: A geometric model: Scientific Reports, v. 8, p. 1–7, doi:10.1038/s41598-018-19152-0.

Sun, Y., Joachimski, M.M., Wignall, P.B., Yan, C., Chen, Y., Jiang, H., Wang, L., and Lai, X., 2012, Lethally hot temperatures during the Early Triassic greenhouse: Science, v. 338, p.

366–370, doi:10.1126/science.1224126.

Tian, L., Bottjer, D.J., Tong, J., Li, F., Yang, T., Song, H., Song, H., and Liang, L., 2015, Distribution and size variation of ooids in the aftermath of the Permian–Triassic mass extinction: Palaios, v. 30, p. 714–727, doi:10.2110/palo.2014.110.

Trower, E.J. et al., 2018, Active ooid growth driven by sediment transport in a high-energy shoal, Little Ambergris Cay, Turks and Caicos Islands: Journal of Sedimentary Research, v. 88, p. 1–20, doi:10.2110/jsr.2018.59.

Trower, E.J., Lamb, M.P., and Fischer, W.W., 2017, Experimental evidence that ooid size reflects a dynamic equilibrium between rapid precipitation and abrasion rates: Earth and Planetary Science Letters, v. 468, p. 112–118, doi:10.1016/j.epsl.2017.04.004.

Walter, L.M., and Morse, J.W., 1984, Reactive surface area of skeletal carbonates during dissolution: Effect of grain size: Journal of Sedimentary Research, v. 54, p. 1081–1090, doi:10.1306/212f8562-2b24-11d7-8648000102c1865d.

Zhong, S., and Mucci, A., 1989, Calcite and aragonite precipitation from seawater solutions of various salinities: Precipitation rates and overgrowth compositions: Chemical Geology, v. 78, p. 283–299, doi:10.1016/0009-2541(89)90064-8.